Compositionally graded AlxCoCrFeNi high-entropy alloys manufactured by laser powder bed fusion

Fengxia Wei[1,#], Siyuan Wei[2,#], Lau Kwang Boon[1], Wei Hock Teh[1], Jing Jun Lee[1], Hwee Leng Seng, Cheng Cheh Tan [1,], Pei Wang [1,3,]*, Upadrasta Ramamurty[1,2,]*

[1]*Institute of Materials Research and Engineering, Agency for Science Technology and Research, Singapore, 138634, Republic of Singapore*

[2]*School of Mechanical and Aerospace Engineering, Nanyang Technological University, Singapore 639798, Republic of Singapore*

[3]*Engineering Cluster, Singapore Institute of Technology, 10 Dover Drive, Singapore 519961, Republic of Singapore*

*Corresponding authors: wangp@imre.a-star.edu.sg, uram@ntu.edu.sg

[#] These authors contribute equally

Abstract: High entropy $Al_xCrCoFeNi$ ($0< x \leq 0.9$) alloy coupon with one dimensional compositionally graded structure was fabricated by laser powder bed fusion using *in situ* alloying of blended metal powders. The chemical composition, crystal structure, microstructure and mechanical properties are studied point by point to investigate the effect of Al constituent. This work deployed a 'semi-high throughput' approach to study the evolution of high entropy alloys and can provide numerous data for accelerated materials discovery using machine learning.

Keywords: high entropy alloy; laser powder bed fusion; phase; microstructure; compositional graded alloy.

---

1. Introduction

The discovery of conventional functional materials is mainly based on 'trial and error' through design of experiment methods. The long time span of such approach becomes one of the major limitations for materials-based technology innovation[1]. The recent emerging 'data-driven' approach facilitated by the advances of high performance computing, is expected to significantly speed up this process. The cornerstone of this new approach is the availability of large amount of data. Additive manufacturing (AM), with in-situ alloying feature and fast fabrication speed, provides a path for accelerated materials screening, particularly for metal alloys.

Laser based AM techniques adopt layer by layer fabrication process, allowing the composition variations during the deposition thus enabling compositionally graded alloy synthesis within short time[2]. There are generally two major types of laser-based AM processes: the laser engineered net shaping (LENS) (i.e. directed energy deposition, DED) and the laser powder bed fusion (L-PBF). The difference between LENS and L-PBF lies on the deposition mode. In LENS, a layer is built by point to point deposition and laser melting, therefore, composition gradient along multiple directions can be easily achieved. Whereas for L-PBF, powder layer with tens to thousands of micrometers thickness is deposited, and laser beam scans the powder along preset paths, thus graded compositions along the building direction can be readily manufactured.

High entropy alloys (HEAs), consisting of at least five different metal elements in high concentrations (5 – 35 at%), have created a new field of metallurgy[3, 4], unlike the conventional alloys which always possess a single dominant element, such as Fe in stainless steels. HEAs could exhibit exceptional properties through the combinations of different constituents. For example, the CrMnCoFeNi alloy as one of the first discovered HEAs, shows extraordinary strength, ductility and fracture toughness at cryogenic conditions[5]. The TiZrHfNbTa HEA exhibits high strength at high temperatures and it can even be cold rolled for microstructure refinement, which represents a big advance for refractory alloys[6]. The large compositional space to be tuned for different properties can be practically limitless[7]. In these circumstances, AM process becomes especially advantageous to quickly fabricate materials with multi-dimensional composition gradients and explore their properties to accelerate the alloy screening.

Aluminum alloys are widely used for their light weight, high strength, and relative low cost. L-PBF fabrication of Al alloys has been challenging because of their porosity and cracks arising from the melting/solidification dynamics during the manufacturing process[8, 9]. Large amount of

efforts have been attempted to enhance the printability of Al alloys, such as the usage of secondary particulates, e.g., Sc or Zr, for grain refinement[9]. Al-containing HEAs are expected to show excellent combination of high strength and low density. The casted $Al_{0.45}CrCoFeNi$ exhibits remarkable yield strength of ~ 1223 MPa but very little ductility after annealed at 700°C for 1 hour, which can be further optimized by post-processing[10]. The structural evolution, *i.e.* the face centered cubic (FCC), body centered cubic (BCC), and primitive cubic (B2) phase formation, with respect to Al content is of great research interests due to their strong influences on mechanical properties. Most of the previous studies are for casted alloys with several selected compositions[10-12]. A thorough investigation on its compositional engineering can shed a light on the future materials design of Al-HEAs.

In this work, we used L-PBF process to manufacture Al-graded HEAs containing Cr, Co, Fe and Ni, and combined the automatic micro-X-ray diffraction (XRD) for crystal structure characterization, large area mapping (LAM) from electron backscattered diffraction (EBSD) for microstructure investigation, electron dispersive spectroscopy (EDS) for composition determination, with the micro-hardness testing and nanoindentation for mechanical property measurement, to perform 'high throughput' alloys screening to investigate the effect of Al contents on structural evolution, and to obtain the optimized compositions for desired mechanical properties.

2. Materials and methods

2.1 Fabrication of compositionally graded alloy

Nitrogen gas atomized CoCrFeNi pre-alloyed powders (average diameter 11.9 ± 5.87 μm) and commercially available Al powders (average diameter 26.9 ± 12.7 μm) are used to fabricate stepwise graded $Al_xCrCoFeNi$ coupons on SS 316L substrate. The mixtures of Al and CrCoFeNi powders (according to 10 compositions shown in Table 1) were blended in roller milling for 24 h and then air-dried before being utilized in TRUMPF TruPrint 1000 model L-PBF machine. A 10 × 10 × 30 mm (width, thickness and height, respectively) sample was started by printing a 3 mm high block on the substrate with first composition, then followed by another 3 mm on top with the next composition and so on. Following optimized fabrication strategy and parameters are used: laser power 120 W, layer thickness 20 μm, hatch spacing 100 μm, scanning speed of 200 mm/s, chess board scanning with island size of 4 × 4 mm and rotation of 67° between successive layers.

The fabricated graded alloy is sectioned along the building direction (BD) and then mechanically polished to a mirror finish for subsequent examination.

2.2 Microstructural and mechanical characterization

The variations of phase, chemical distribution and microstructure are examined by X-Ray diffraction (XRD, Bruker D8 Discover) with a Cu source (λ = 1.54016 Å), energy-dispersive X-Ray spectroscopy (EDS), backscattered electron (BSE) imaging and electron backscatter diffraction (EBSD) with inverse pole figure (IPF) mapping using scanning electron microscopy (SEM, JEOL 7600 F). The quantitative crystal structure analysis was performed by TOPAS v5 software via batch mode Rietveld refinements using fundamental parameters peak profile function, applying the FCC ($Fm\bar{3}m$), BCC ($Im\bar{3}m$) and B2 ($Pm\bar{3}m$) crystal information as input. Random atomic distributions are assumed for FCC and BCC phases, and CrCoFeNi (0, 0, 0), Al (0.5, 0.5, 0.5) are used for B2. Both Vickers microhardness testing and nano-indentation (Agilent G200 Nanoindenter XP) were utilized to examine the mechanical responses of the graded alloy. Nanoindentations with a Berkovich tip were conducted for each region with a peak depth of 1000 nm, a hold time of 10s and loading/unloading rates of 10 nm/s.

3. Results

3.1 Microstructures

The average chemical composition of each region is listed in Table 1. The compositional variation of Al is plotted against locations in the graded samples, as demonstrated in Fig. 1a. As seen from it, a step-wise gradient of Al is created along the BD. Moreover, as examined by the EDS mapping across the whole sample, it is shown that in the as-printed Al-HEA graded samples, all the elements are homogeneously distributed, where no evident chemical segregation can be seen. As an example, the elemental mapping of the region with the maximum Al content is shown in Fig. 1b-c; the randomly distributed elemental components indicate the well mixing of the powders.

Table 1. The nominal (*N*) and measured (*M*) average chemical compositions of 10 regions (all in at.%).

Region			Co	Cr	Fe	Ni	Al
1	$Al_{0.1}CoCrFeNi$	*N*	24.4	24.4	24.4	24.4	2.4
		M	24.8	24.6	24.7	24.0	1.8

2	$Al_{0.2}CoCrFeNi$	*N*	23.8	23.8	23.8	23.8	4.8
		M	24.7	24.0	24.0	23.8	3.5
3	$Al_{0.3}CoCrFeNi$	*N*	23.3	23.3	23.3	23.3	7.0
		M	23.9	23.4	23.6	23.0	6.2
4	$Al_{0.4}CoCrFeNi$	*N*	22.7	22.7	22.7	22.7	9.1
		M	23.5	22.9	23.2	22.9	7.5
5	$Al_{0.5}CoCrFeNi$	*N*	22.2	22.2	22.2	22.2	11.1
		M	23.3	22.3	22.8	22.4	9.3
6	$Al_{0.6}CoCrFeNi$	*N*	21.7	21.7	21.7	21.7	13.0
		M	22.6	22.2	22.4	21.7	11.1
7	$Al_{0.7}CoCrFeNi$	*N*	21.3	21.3	21.3	21.3	14.9
		M	22.4	21.7	22.1	21.5	12.3
8	$Al_{0.8}CoCrFeNi$	*N*	20.8	20.8	20.8	20.8	16.7
		M	21.7	21.3	21.7	21.1	14.3
9	$Al_{0.9}CoCrFeNi$	*N*	20.4	20.4	20.4	20.4	18.4
		M	21.3	20.9	21.1	20.4	16.3
10	AlCoCrFeNi	*N*	20.0	20.0	20.0	20.0	20.0
		M	21.0	20.4	20.6	19.9	18.1

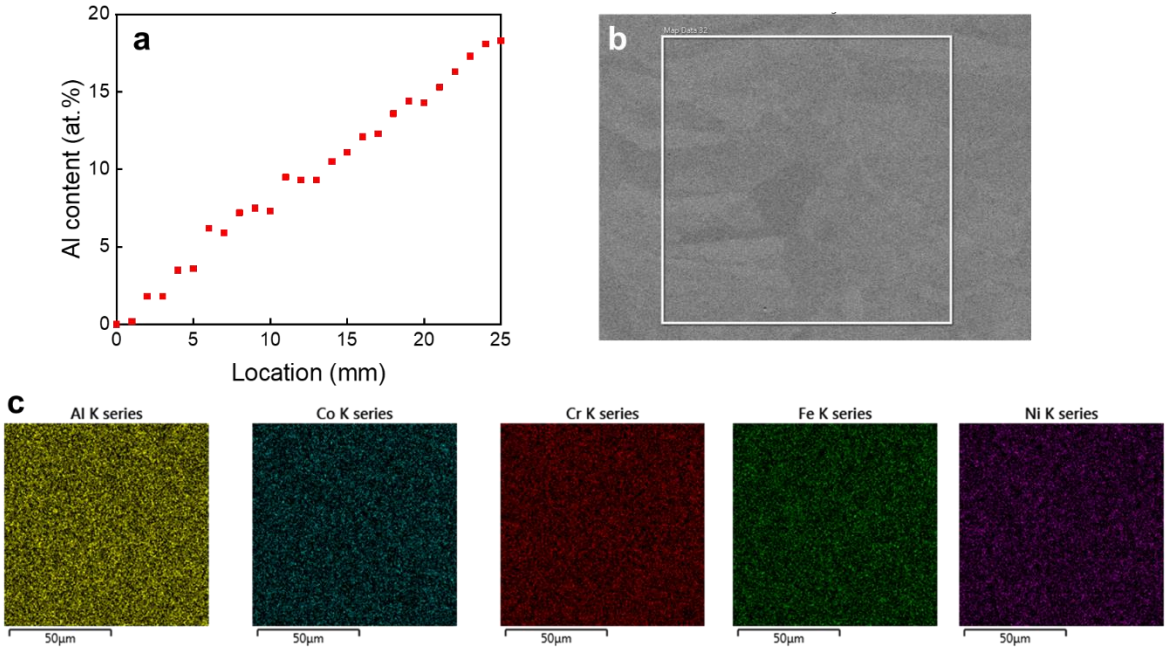

Figure 1. Characterizations of Al in the graded AlxCoCrFeNi samples. (a) variation of Al along the gradient direction, measured by EDS. (b) Backscattered electron (BSE) image and elemental mappings (c) for the position containing the highest Al concentration (~18.1 at%).

Porosity and cracks are the two main challenges for all the AM process. Here, one objective of this work is to examine the maximum Al content in CoCrFeNi HEA during L-PBF fabrication. The porosities are 0.42%, 1.19%, 3.47%, 9.59% and 9.05% in region 1-10, respectively. The porosity drastically increased with increasing Al content. Sun *et. al.* reported three separate compositions of L-PBF fabricated $Al_xCrCoFeNi$ (x = 0.1, 0.5 and 1), and found severe hot cracking in all the samples, which exhibits a nonlinear relationship between the amount of cracks and the Al content [13]. However, in our graded sample, the cracking is only observed in regions with comparatively high Al content ($Al_xCrCoFeNi$, $x \geq 0.6$) where the brittle BCC phase dominates. Therefore, it is postulated that this graded fabrication methodology suppressed the formation of hot cracking in the FCC regions. Due to the differences in atomic radius and thermal-expansion ratio between Al and Cr, Co, Fe, Ni, increasing Al contents resulted in the buildup of internal stress during solidification. To examine such effect, same range of Al content is incorporated in CoCrFeNi, while reducing the gradient steps from 10 to 5, it is found that crack formation is effectively suppressed.

The variation of microstructures and phases across the graded alloy, examined by EBSD, is shown in Fig. 2. From region 1 to region 6 (1.8 – 11.1 at.% Al), large columnar grains with predominant <110> orientation can be seen. These regions are exclusively comprised of FCC phase (Fig. 2c). When the Al content reaches (12.3 at.% Al) in region 7, an abrupt refinement of grain size is spotted, which should be induced by the occurrence of BCC phase (Fig. 2c). Further increase of Al content results in dominance of BCC phase; and finally in region 10 (18.1 at.% Al), significant refinement of the grains and randomization of their orientations are observed. The representative texture (regions 1, 7, 8 and 10) evolution in the fabricated coupon with the Al content is illustrated in Fig. 3 through pole figures obtained at each of the locations and on cross-sections normal to BD. It is interesting to note that the regions 1-6 and regions 8-9 all show evident textures, yet the dominant orientations are different; regions 1-6 are <110>-textured, while the grains in regions 8-9 are markedly aligned towards <100> orientation. With regard to regions 7 and 10, no significant texture can be seen.

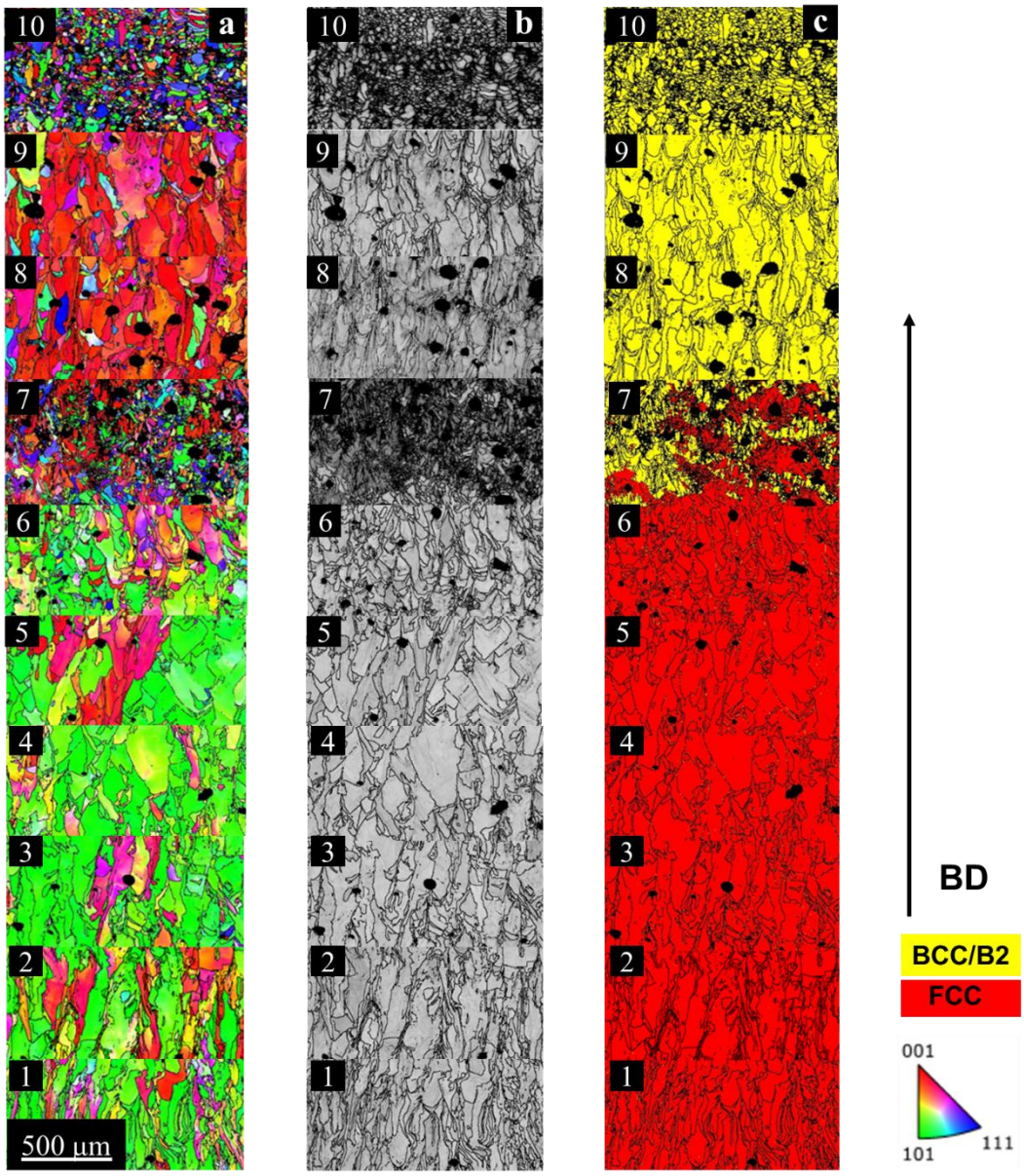

Figure 2. (a) Electron backscatter diffraction (EBSD) inversed pole figures (IPF), (b) backscattered electron (BSE) images and (c) phase images showing the microstructural variation across the entire graded coupon along the build direction (BD).

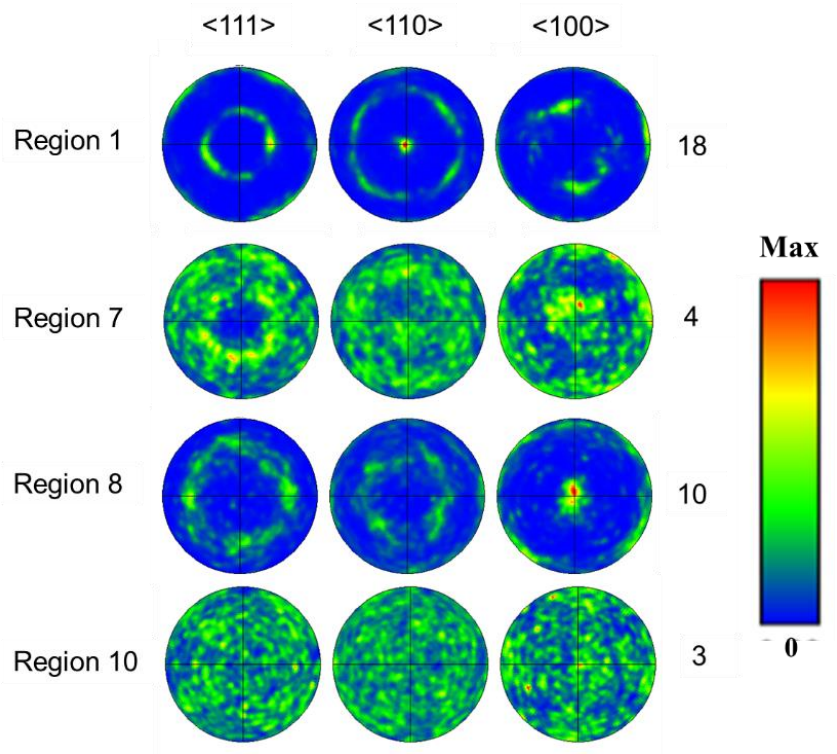

Figure 3. The pole figures of region 1, 7, 8 and 10 along building direction. Numbers on the right-hand side show the maximum intensity of each IPF figure.

XRD is further used to quantitively examine the phase compositions in $Al_xCrCoFeNi$ graded samples (Fig. 4). Other than FCC and BCC phases that are readily spotted in EBSD, an intermetallic phase B2 can also be seen. The atomic arrangements of three phases are schematically shown in Fig. 4d. FCC and BCC phases are disordered solid solution with atoms randomly distributed in the lattice structure, while B2 phase has fixed atomic arrangements. The XRD patterns obtained from each of the ten regions are displayed in Fig. 4b. Analysis of these patterns shows that: (i) FCC phase is exclusively found in regions 1-6, (ii) FCC and BCC phase co-exist in region 7, and (iii) BCC and B2 phases are seen in regions 8-10. It is observed that the evolution of lattice structures is closely related to the Al content (Fig. 4c). More specifically, single FCC phase can be readily obtained for Al less than 9.5 at.%, while BCC phase is captured when Al increased to 10.5 at.%. Small amount of the ordered B2 phase is spotted by XRD when Al content > 12.1 at.%. BCC quickly dominated for Al > 13.6 at.%, and eventually contributed to more than 99 wt.% of the sample. This evolution is in good agreement with the casted $Al_xCrCoFeNi$ [14].

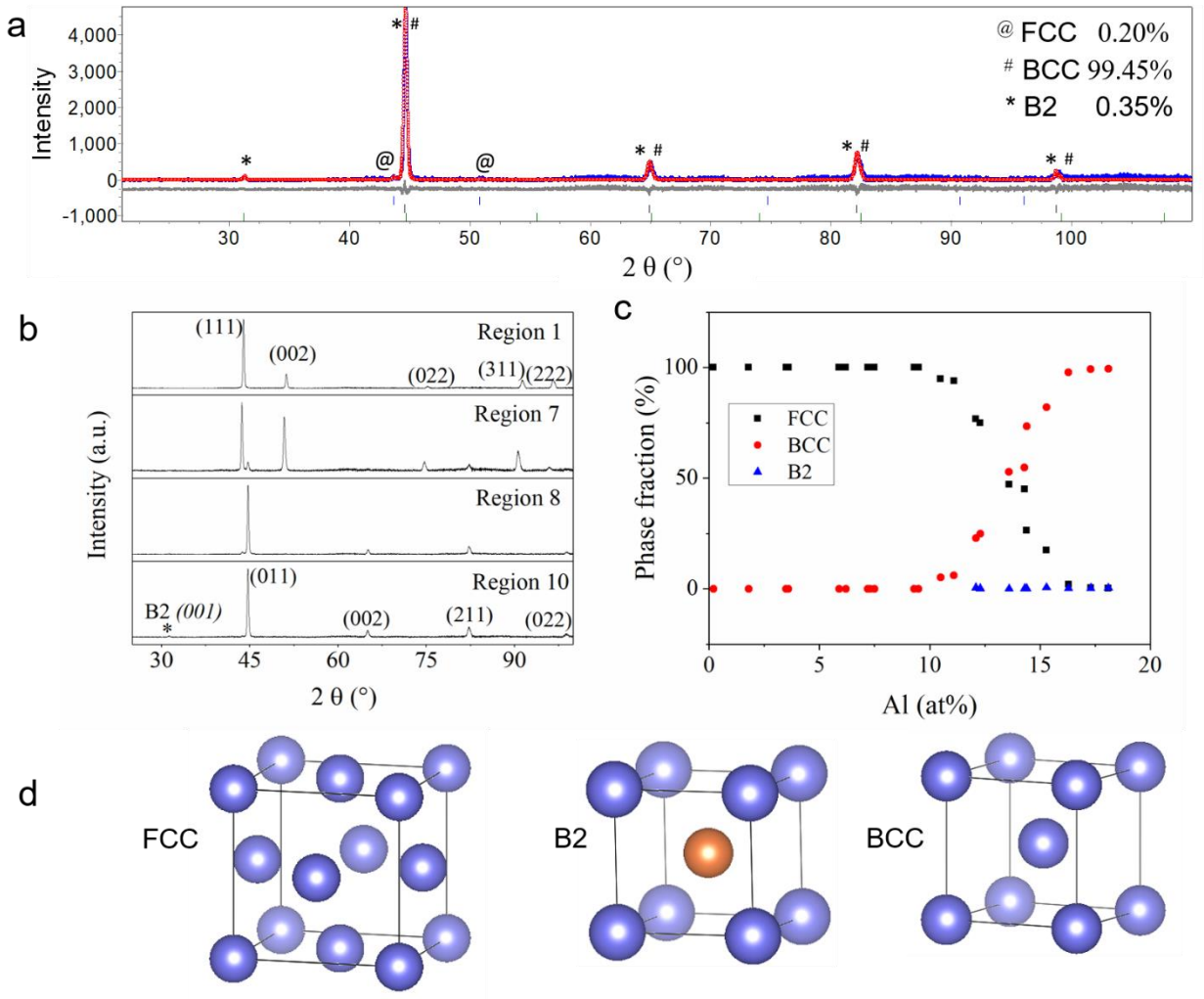

Figure 4. (a) An example of XRD Rietveld refinement for tip of region 10, with approximate composition $Al_{0.18}Cr_{0.20}Fe_{0.21}Co_{0.21}Ni_{0.20}$, calculated phase weight ratio is as indicated in the legend. Blue: experimental, red: calculated, grey: differences. (b) Selected XRD patterns obtained from different regions along the building direction. Region 1 is FCC, region 10 is mainly BCC + B2. (c) The phase fraction as a function of Al at.% from Rietveld analysis. (d) Schematic illustrations of FCC, BCC and B2 structures.

The average grain sizes for different regions are similar to each other (Table 2), except for the region 7 where FCC and BCC co-exist, and region 10 with high Al content ($x > 0.8$) where grain shapes turn regular. At low Al contents ($x < 0.5$), strong texture can be observed throughout the coupon due to relatively big columnar grains, but the texture doesn't show any obvious correlations with Al contents. BCC starts to emerge in the grain boundaries of FCC phases (Fig. 2), serving as nano-precipitates to enhance the mechanical properties. The emergency of BCC created a fine grain area (region 7), but grains tend to merge after BCC phase is stabilized.

Compositions with high Al contents (x > 0.8) at the end of the sample possesses random grain orientations and refined microstructures, which is a combined effect of composition and less heating/cooling cycles during the printing. Although the effect of Al on grain sizes and textures are not apparent, the dislocation densities show a clear dependency. In general, the geometrical necessary dislocations (GNDs) measured by EBSD decrease with increasing Al contents (Table 2, Figure S3), except the transition regions from regions 5 to 8 where FCC dominant turns into BCC dominant. A total GND local minima is present at region 7 with the FCC/BCC bilayers. FCC is a close packing structure exhibiting higher packing efficiency compared to BCC. The FCC to BCC phase transitions tend to release the internal stresses due to atomic size mismatch between Al and parent metals, thus GNDs decrease. After BCC becomes dominating, further increasing Al ratio would accumulate more stress, resulting in more dislocations. The significant reduction in region 10 could be related to the heating cycles during the fabrication as well as the presence of B2 phase.

Table 2. The grain size and GND distributions.

	GND (10^{14}/m^2)				Grain size (μm)			
Region	FCC	std	BCC/B2	std	FCC	std	BCC	std
1	0.99	0.50	1.14	0.74	27.40	34.76		
2	0.87	0.48	1.06	0.70	27.40	40.72		
3	0.74	0.44	1.09	0.65	31.39	46.77		
4	0.60	0.38	1.09	0.65	30.47	43.97		
5	0.52	0.34	1.03	0.59	27.50	33.89		
6	0.54	0.34	1.05	0.55	25.08	30.30		
7	0.54	0.32	0.71	0.37	15.91	16.10	13.15	10.27
8	0.65	0.35	0.65	0.40			28.55	34.93
9	0.65	0.34	0.58	0.42			25.62	31.51
10	0.60	0.34	0.41	0.29			15.77	11.24

3.2 Mechanical Properties

Variations of elastic modulus (E), micro-hardness (H) and nano-indentation hardness (NH) are plotted against Al content in Fig.7. According to the results in Fig.5c, pure FCC, FCC + BCC and pure BCC regions are marked out. In the pure FCC region (< 10 at.% Al), a near linear decreasing of E can be seen. When BCC phase starts to form, E markedly increases; with increasing Al content, E drops again in the FCC + BCC and pure BCC regions. Both H and NH show similar trends with increasing Al, despite that NH is constantly higher than H (size effect of indentation depth). More specifically, both H and NH increase, slightly in pure FCC region (< 10 at.% Al) and then steeply

after BCC-formation occurs. After achieving maximum hardness (NH ~ 7.8 GPa, H ~ 579 Hv0.3) at 17.3 and 15.3 at.% Al, respectively, values of both NH and H drop with further Al increasement, presumably due to the cracking.

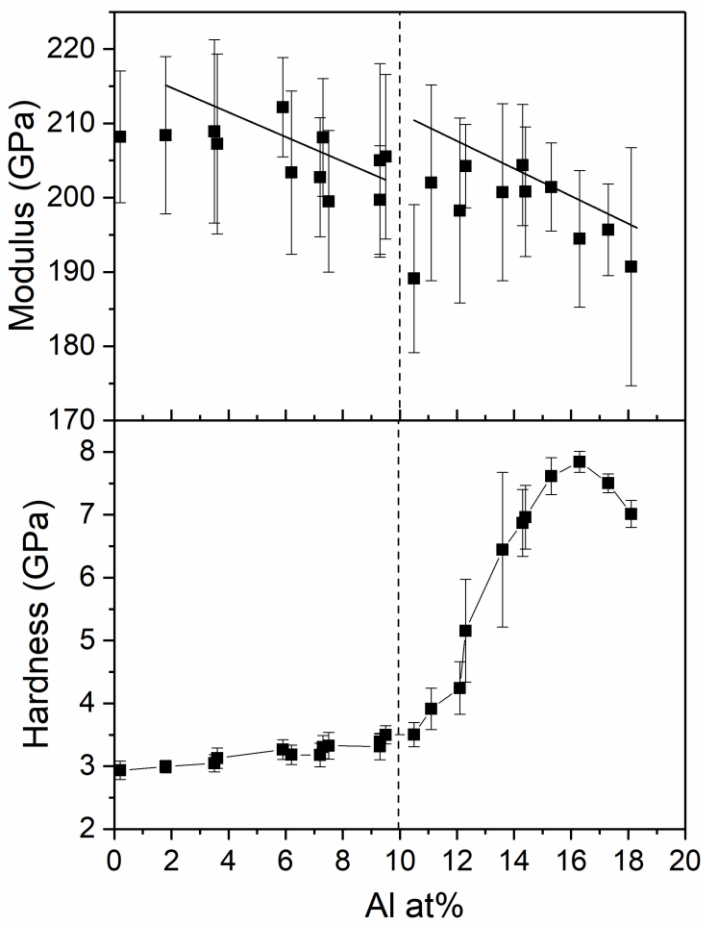

Figure 7. Variations of Young's modulus (*E*) and hardness values measured with nanoindentation (NH) with the Al content along the gradation. These mechanical properties were measured on the planes with the plane-normal oriented perpendicular to the build direction (BD). Dashed lines mark out the Al content where BCC phase starts to form.

4. Discussion

4.1 Effects of Al on the microstructure and mechanical properties of L-PBF HEAs

It is well accepted that Al acts as a strong BCC stabilizer in conventionally manufactured HEAs [12, 14-16], where Al addition induced FCC to BCC phase transitions have been widely investigated. Based on Hume–Rothery rules, it is proposed that the criteria for achieving solid

solution phase is determined by two dominating parameters, *i.e.*, enthalpy of mixing (ΔH_{mix}) and difference in atomic radius (δ)[17]:

$$\Delta H_{mix} = 4\sum_{i=1,i\neq j}^{n} \Delta H_{ij}^{mix} c_i c_j \quad (1)$$

$$\delta = \sqrt{\sum_{i=1}^{n} c_i (1 - \frac{r_i}{\bar{r}})^2} \quad (2)$$

where c_i is the atomic ratio of the *i*th element, ΔH_{ij}^{mix} the enthalpy of mixing between element *i* and *j*, r_i the atomic radius of *i*th element. Following above criteria, disordered solid solution in HEAs can be achieved when -15 < ΔH_{mix} < 5 kJ/mol and 1 < δ < 5% [18]. However, such criteria can only be applied to predict the existence of ordered intermetallics and disordered solid solution; it is insufficient to describe the phase evolution from the single disorder FCC solid solution to the mixture of FCC and BCC, and to the single BCC phase. To further predict the transition of disorder solid solution phase, valence electron concentration (VEC) is proposed[19]:

$$VEC = \sum_{i=1}^{n} c_i \, VEC_i \quad (3)$$

where VEC_i is the VEC value for the *i*th element. The VEC for Al, Co, Cr, Ni and Fe are 3, 9, 6, 10 and 8, respectively. The estimated VEC values across the Al gradation in the current study are displayed in Fig. 8. According to the VEC criterion [15, 20], FCC phases are stable at higher VEC ($\geqslant$8) whereas BCC phases are stable at lower VEC (<6.87). As seen from Fig.8, the VEC linearly decreases with increasing Al, indicating that the Al addition gradually promotes covalency. However, despite that FCC+BCC structure falls within the predicted region, the VEC criterion obviously offers a wider range for forming the single FCC and BCC solid solution phases, as compared with the experimental data. This observation indicates that atomic bonding is not the only dominant factor in phase formation of AlxCrCoFeNi HEAs. Similar phenomenon is also reported in conventionally manufactured samples[15].

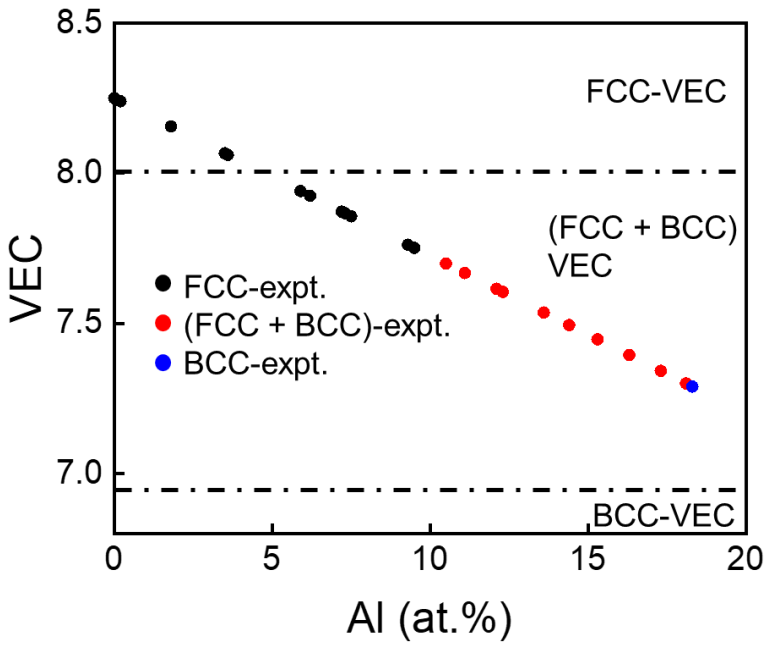

Figure 8. The value of valence electron concentration (VEC) as a function of the Al content in AlxCrCoFeNi graded alloys. Dashed lines mark out the FCC, FCC+BCC and BCC stable region, based on VEC criteria.

To further discuss the possible factor that affects phase formation and the effect of unique thermal conditions during L-PBF, we plotted the fraction of BCC phase against Al content in AlxCrCoFeNi of different conditions (Fig. 9), *i.e.*, as fabricated by L-PBF (this study), as-cast and homogenized (obtained from literature [14]). As seen from it, variations of BCC phases against Al content in L-PBF and as-cast samples show similar trend: relatively narrow range of duplex region (9.3 -18.3 at.% Al in L-PBF, 7.8 -16.2 at.% Al in as-cast samples) and thusly steep transition from FCC to BCC. Based on the above discussion, it can be seen that transition of disorder phases is closely related to VEC, which is exclusively controlled by element content. Therefore, BCC-Al content plots of L-PBF and as-cast samples should be similar, despite the disparate thermal conditions. However, when samples are exposed to long-time homogenization (1100 ℃ for 24 h), the duplex region is markedly wider (8.0 -25.5 at.% Al) than the as-fabricated samples (both L-PBF and casting). It is known that the cooling rate in L-PBF (10^5– 10^6 K/s [21, 22]) is characteristically higher, compared to casting (typically 10^0– 10^2 K/s [21, 23]); yet they both facilitate the transition from FCC to BCC. This indicates that VEC is not the only reason for phase transition in AlxCoCrFeNi.

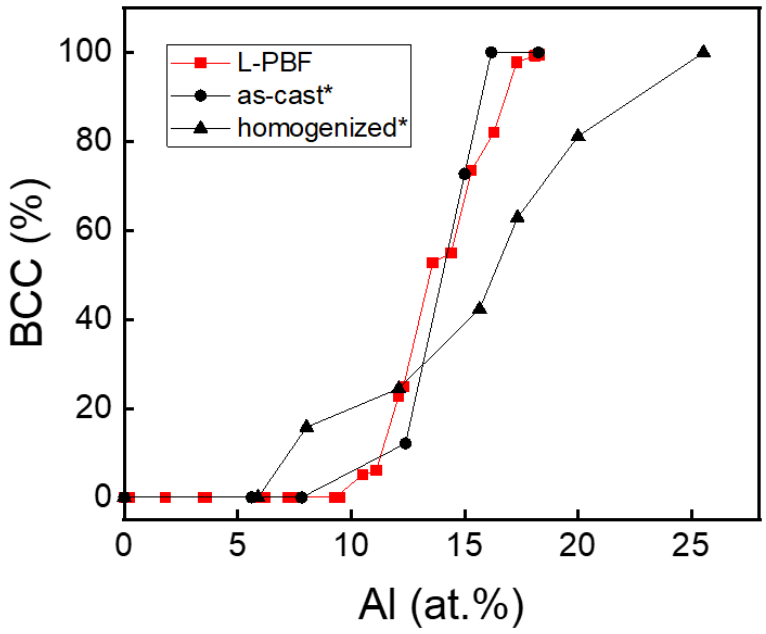

Figure 9. Variations of fractions of BCC phase with Al content in AlxCrCoFeNi samples as fabricated by L-PBF, as-cast and homogenized. *Data obtained from literature [14].

The lattice parameters (LPs) of AlxCoCrFeNi alloy are closely related to Al content, due to its evidently larger atomic radius than other elements. Therefore, based on the variation of LP, we can inversely postulate the preferred locations of Al. In the FCC region, LPs exhibit a proportional dependency on the Al at%, shown as peak shift to smaller 2θ in Fig. 4, indicating a homogeneous solid solution. With the emerging of BCC, LPs of FCC decrease at first then increase, probably because that Al preferably stays in the BCC than FCC lattices, and the at.% of Al in FCC decreased upon BCC nucleation. LPs show inverse proportionality correlation with Al in the FCC+BCC+B2 region where B2 starts to precipitate, which means Al atoms preferably reside at B2 than BCC lattices. The amount of FCC reduced dramatically and when BCC dominates, LPs tend to increase again with increasing Al. These findings can be further verified by the *in situ* TEM study on $Al_xCrCoFeNi$, where the so-called $Al_{0.7}CrCoFeNi$ is actually composed of $Al_{4.0}Cr_{25.0}Cr_{28.8}Fe_{28.9}Ni_{13.3}$ (FCC), $Al_{4.6}Cr_{18.8}Cr_{44.5}Fe_{27.4}Ni_{4.7}$ (BCC) and $Al_{40.1}Cr_{12.7}Cr_{3.6}Fe_{3.6}Ni_{40.0}$ (B2) at 900 °C [11]. Therefore, Al atoms have preference of B2 over BCC and BCC over FCC, the molecular compositions tend to show a trend where $Al_{B2} > Al_{BCC} > Al_{FCC}$.

The BCC phases' formation originated from the grain boundaries (EBSD), as shown in Fig. 10. Then the grain started to grow and consumed the FCC grains. A bilayer transition region (*i.e.*, region 7 in Fig. 2) was formed where BCC suddenly dominated due to high Al concentration, but was quickly replaced by the FCC phase which was then conquered by BCC again, leading to a stable BCC dominating region. This is probably due to the competitions between their formation enthalpies and the fabrication conditions, large pores were also resulted.

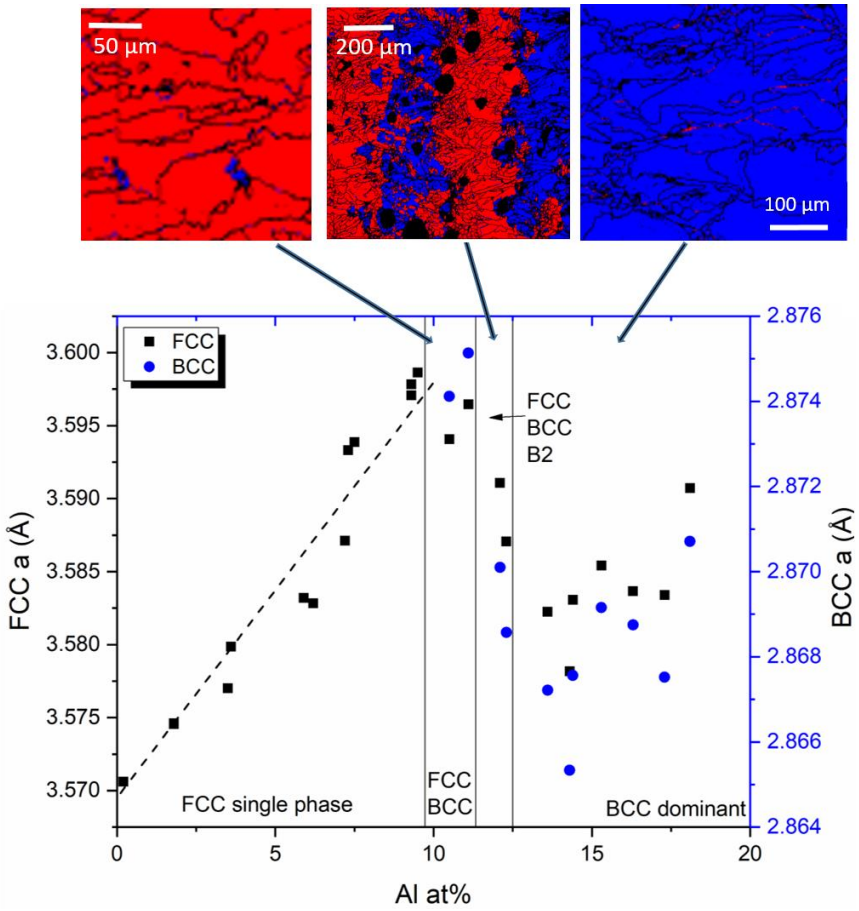

Figure 10. Lattice parameters variation as a function of Al content, and the EBSD phase maps obtained from regions 6, 7 and 9, respectively. Phase identity: red for FCC, blue for BCC. Scales are different for better illustrations.

4.2 AM-enabled high throughput materials screening

A major challenge facing metal AM is the limitation of alloys available as (i) the raw material should be available in the powder form and (ii) the alloy should be amenable to AM without cracking. Currently, there has been extensive work done on L-PBF fabricated metallic parts, but

most of the alloys explored are those designed for conventional methods. Hence, metal L-PBF is still in its nascent stage, with the exploration of new alloy chemistries and/or fabrication of components with unique functional and/or mechanical properties being relatively unexplored. For the former, in-situ alloying offers significant potential in terms of exploring the composition-microstructure-property relationship by easily adjusting the powder feedstock mixtures.

Here, we reported a practical example of L-PBF enabled rapid alloy screening in AlxCoCrFeNi. The large composition variations for multiple constituents in HEA make it challenging for exhaustive experimental examination by casting. Our present work showcases a simple way of printing one dimensionally graded Al-HEA using L-PBF; combining micro-XRD, large area mapping in EBSD and mechanical characterization, the printability, microstructure and mechanical properties of 10 different compositions can be examined in one printing job. Moreover, significant amount of data can be generated, including the information about printing parameters, compositions, crystal structures, microstructures, hardness and Young's modulus. Two dimensional composition gradient alloy fabrication can also be realized (patent no.), which further enlarges the number of training data that can be provided for machine learning.

5. Summary

In this work, we fabricated compositional graded $Al_xCrCoFeNi$ ($0< x \leq 1$) using L-PBF, performed in-depth investigations on their crystal structure evolution, microstructure variation and mechanical properties enhancement. The following findings are concluded:

(1) Crystal structure evolutions show good agreement with the casted counterparts, but AM fabrication can provide more details with much smaller composition step size:
   (a) $0 < Al < 0.47$, pure FCC phase;
   (b) $0.47 \leq Al \leq 0.56$, FCC+BCC, FCC dominates, B2 nucleates at $x = 0.55$;
   (c) $0.63 \leq Al \leq 0.78$, BCC+FCC+B2, BCC dominates;
   (d) $0.84 \leq Al \leq 0.90$, BCC+B2, trace amount of FCC.
   (e) Al shows crystal structure preferences: B2 > BCC > FCC.

(2) Grain size and texture don't show obvious correlations with compositions, but GNDs tend to decrease with increasing Al content. An area with refined grains at the top of coupon

(end of the printing) with low dislocation density is obtained at high Al content, suggesting the heating and cooling cycles during the L-PBF process are the main origins of cellular structures and dislocations.

(3) Elastic modulus tends to reduce with increasing Al for both FCC and BCC phases, this is because introduction of Al with larger atomic size but less delocalized electrons elongates the bond length, weakens the bond strength.

(4) Hardness increases with increasing Al in general. Highest hardness is obtained when BCC reaches ~ 98 wt.%. The hardness reduction at the end of sample mainly arises from the low dislocation density.

(5) Multi-dimensional composition gradient fabrication can be realized by AM method, which significantly speeds up the researches for HEAs. It can also provide numerous data points for the accelerated materials research using machine learning.

Acknowledgement

This work is funded by the Structural Metal Alloys Program (Grant reference No. A18b1B0061) of the Agency for Science, Technology and Research of Singapore. The authors gratefully thank the technical support nanoindentation measurement by Mr. Tzee Luai Meng of IMRE.

References:

[1] J.M. Cole, A Design-to-Device Pipeline for Data-Driven Materials Discovery, Acc. Chem. Res. 53 (2020) 599-610, 10.1021/acs.accounts.9b00470.
[2] C. Zhang, F. Chen, Z. Huang, M. Jia, G. Chen, Y. Ye, Y. Lin, W. Liu, B. Chen, Q. Shen, L. Zhang, E.J. Lavernia, Additive manufacturing of functionally graded materials: A review, Mater. Sci. Eng. A 764 (2019), 10.1016/j.msea.2019.138209.
[3] J.W. Yeh, S.K. Chen, S.J. Lin, J.Y. Gan, T.S. Chin, T.T. Shun, C.H. Tsau, S.Y. Chang, Nanostructured high‐entropy alloys with multiple principal elements: novel alloy design concepts and outcomes, Adv. Eng. Mater. 6 (2004) 299-303, 10.1002/adem.200300567.
[4] B. Cantor, I.T.H. Chang, P. Knight, A.J.B. Vincent, Microstructural development in equiatomic multicomponent alloys, Mater. Sci. Eng. A 375-377 (2004) 213-218, 10.1016/j.msea.2003.10.257.
[5] B. Gludovatz, A. Hohenwarter, D. Catoor, E.H. Chang, E.P. George, R.O. Ritchie, A fracture-resistant high-entropy alloy for cryogenic applications, Science 345 (2014) 1153-1158, 10.1126/science.1254581.
[6] C.-C. Juan, M.-H. Tsai, C.-W. Tsai, W.-L. Hsu, C.-M. Lin, S.-K. Chen, S.-J. Lin, J.-W. Yeh, Simultaneously increasing the strength and ductility of a refractory high-entropy alloy via grain refining, Mater. Lett. 184 (2016) 200-203, 10.1016/j.matlet.2016.08.060.
[7] E.P. George, D. Raabe, R.O. Ritchie, High-entropy alloys, Nat. Rev. Mater. 4 (2019) 515-534, 10.1038/s41578-019-0121-4.
[8] J.H. Martin, B.D. Yahata, J.M. Hundley, J.A. Mayer, T.A. Schaedler, T.M. Pollock, 3D printing of high-strength aluminium alloys, Nature 549 (2017) 365-369, 10.1038/nature23894.
[9] N.T. Aboulkhair, M. Simonelli, L. Parry, I. Ashcroft, C. Tuck, R. Hague, 3D printing of Aluminium alloys: Additive Manufacturing of Aluminium alloys using selective laser melting, Prog. Mater. Sci. 106 (2019) 100578, 10.1016/j.pmatsci.2019.100578.
[10] J. Hou, Z. Wang, X. Shi, Z. Wang, J. Qiao, Y. Wu, Strengthening of an Al0.45CoCrFeNi high-entropy alloy via in situ fabricated duplex-structured composites, J. Mater. Sci. 55 (2020) 7894-7909, 10.1007/s10853-020-04550-5.
[11] J.C. Rao, H.Y. Diao, V. Ocelík, D. Vainchtein, C. Zhang, C. Kuo, Z. Tang, W. Guo, J.D. Poplawsky, Y. Zhou, P.K. Liaw, J.T.M. De Hosson, Secondary phases in AlxCoCrFeNi high-entropy alloys: An in-situ TEM heating study and thermodynamic appraisal, Acta. Mater. 131 (2017) 206-220, 10.1016/j.actamat.2017.03.066.
[12] W.-R. Wang, W.-L. Wang, S.-C. Wang, Y.-C. Tsai, C.-H. Lai, J.-W. Yeh, Effects of Al addition on the microstructure and mechanical property of AlxCoCrFeNi high-entropy alloys, Intermetallics 26 (2012) 44-51, 10.1016/j.intermet.2012.03.005.
[13] Z. Sun, X. Tan, C. Wang, M. Descoins, D. Mangelinck, S.B. Tor, E.A. Jägle, S. Zaefferer, D. Raabe, Reducing hot tearing by grain boundary segregation engineering in additive manufacturing: example of an AlxCoCrFeNi high-entropy alloy, Acta. Mater. 204 (2021), 10.1016/j.actamat.2020.116505.
[14] Y.-F. Kao, T.-J. Chen, S.-K. Chen, J.-W. Yeh, Microstructure and mechanical property of as-cast, -homogenized, and -deformed AlxCoCrFeNi ($0 \leqslant x \leqslant 2$) high-entropy alloys, Journal of Alloys and Compounds 488 (2009) 57-64, 10.1016/j.jallcom.2009.08.090.
[15] J.Y. He, W.H. Liu, H. Wang, Y. Wu, X.J. Liu, T.G. Nieh, Z.P. Lu, Effects of Al addition on structural evolution and tensile properties of the FeCoNiCrMn high-entropy alloy system, Acta Materialia 62 (2014) 105-113, 10.1016/j.actamat.2013.09.037.
[16] J. Cieslak, J. Tobola, K. Berent, M. Marciszko, Phase composition of AlxFeNiCrCo high entropy alloys prepared by sintering and arc-melting methods, Journal of Alloys and Compounds 740 (2018) 264-272, 10.1016/j.jallcom.2017.12.333.
[17] Y. Zhang, Y.J. Zhou, J.P. Lin, G.L. Chen, P.K. Liaw, Solid‐solution phase formation rules for multi‐component alloys, Advanced engineering materials 10 (2008) 534-538,
[18] T. Egami, Y. Waseda, Atomic size effect on the formability of metallic glasses, Journal of non-crystalline solids 64 (1984) 113-134,

[19] S. Guo, C.T. Liu, Phase stability in high entropy alloys: Formation of solid-solution phase or amorphous phase, Progress in Natural Science: Materials International 21 (2011) 433-446, 10.1016/s1002-0071(12)60080-x.
[20] Y. Zhao, K.B. Lau, W.H. Teh, J.J. Lee, F. Wei, M. Lin, P. Wang, C.C. Tan, U. Ramamurty, Compositionally graded CoCrFeNiTi high-entropy alloys manufactured by laser powder bed fusion: A combinatorial assessment, Journal of Alloys and Compounds 883 (2021), 10.1016/j.jallcom.2021.160825.
[21] T. DebRoy, H.L. Wei, J.S. Zuback, T. Mukherjee, J.W. Elmer, J.O. Milewski, A.M. Beese, A. Wilson-Heid, A. De, W. Zhang, Additive manufacturing of metallic components – Process, structure and properties, Progress in Materials Science 92 (2018) 112-224, https://doi.org/10.1016/j.pmatsci.2017.10.001.
[22] I.A. Roberts, C. Wang, R. Esterlein, M. Stanford, D. Mynors, A three-dimensional finite element analysis of the temperature field during laser melting of metal powders in additive layer manufacturing, International Journal of Machine Tools and Manufacture 49 (2009) 916-923,
[23] J. Elmer, S. Allen, T. Eagar, Microstructural development during solidification of stainless steel alloys, Metallurgical transactions A 20 (1989) 2117-2131,